PROPER MOTIONS AND TRAJECTORIES FOR 16 EXTREME RUNAWAY AND HYPERVELOCITY STARS*

WARREN R. BROWN[1], JAY ANDERSON[2], OLEG Y. GNEDIN[3], HOWARD E. BOND[2,4], MARGARET J. GELLER[1], AND SCOTT J. KENYON[1]
[1] Smithsonian Astrophysical Observatory, 60 Garden St, Cambridge, MA 02138, USA; wbrown@cfa.harvard.edu
[2] Space Telescope Science Institute, 3700 San Martin Dr., Baltimore, MD 21218, USA
[3] Department of Astronomy, University of Michigan, Ann Arbor, MI 48109, USA
[4] Department of Astronomy & Astrophysics, Pennsylvania State University, University Park, PA 16802, USA

ABSTRACT

We measure proper motions with the *Hubble Space Telescope* for 16 extreme radial velocity stars, mostly unbound B stars in the Milky Way halo. Twelve of these stars have proper motions statistically consistent with zero, and thus have radial trajectories statistically consistent with a Galactic center "hypervelocity star" origin. The trajectory of HE 0437–5439 is consistent with both Milky Way and Large Magellanic Cloud origins. A Galactic center origin is excluded at 3σ confidence for two of the lowest radial velocity stars in our sample, however. These two stars are probable disk runaways and provide evidence for $\sim$500 km s^{-1} ejections from the disk. We also measure a significant proper motion for the unbound sdO star US 708. Its 1000 km s^{-1} motion is in some tension with proposed supernova ejection models, but can be explained if US 708 was ejected from the stellar halo. In the future, we expect *Gaia* will better constrain the origin of these remarkable unbound stars.

Key words: Galaxy: halo – Galaxy: kinematics and dynamics – Magellanic Clouds – stars: early-type – stars: kinematics and dynamics

1. INTRODUCTION

The Milky Way is a gravitationally bound system of a few 10^{11} stars, but it also hosts some unbound stars. Where these unbound stars come from is an open question. It is very difficult to explain unbound main-sequence stars by supernova explosions in close binary systems (Blaauw 1961) or by dynamical encounters between binaries (Poveda et al. 1967), the mechanisms that explain disk "runaway" stars. Simulations show that stars cannot be launched at speeds greater than their binary orbital velocity, and this velocity cannot exceed the escape velocity from a star's surface, since that would require the stars to be orbiting inside one another (Leonard 1991). The escape velocity from the surface of main-sequence stars is comparable to the 500–600 km s^{-1} local Galactic escape velocity (Piffl et al. 2014). Only dynamical interactions with an object more massive and compact than a star can easily explain unbound main-sequence stars. Hills (1988) predicted that three-body exchange interactions between stars and the central massive black hole (MBH) will inevitably unbind stars from the Galaxy, and he called such objects "hypervelocity stars" (HVSs). We therefore refer to unbound main-sequence stars in this paper as HVSs.

The first HVS was discovered by Brown et al. (2005), and a couple dozen B-type HVSs are now known in the Milky Way halo (Edelmann et al. 2005; Brown et al. 2006a, 2006b, 2007a, 2007b, 2009, 2012b, 2014; Heber et al. 2008; Zheng et al. 2014). These stars have radial velocities up to +700 km s^{-1}; no star moving toward us with a comparable radial velocity has ever been observed. To date, detailed spectroscopic analyses of the B-type HVSs find that they are main-sequence B stars at 10–100 kpc distances (Edelmann et al. 2005; López-Morales & Bonanos 2008; Przybilla et al. 2008a, 2008b; Brown et al. 2012a, 2013). The short

lifetimes of B stars require that these unbound stars were ejected from a region with recent star formation, such as the Galactic disk or the Galactic center.

Full three-dimensional trajectories for the HVSs are a crucial test of their origin. Measuring the trajectories for the HVSs, however, requires accurate distances and absolute proper motions. Distance estimates to individual stars are determined by comparing either spectroscopic $T_{\rm eff}$ and log g or broadband colors to stellar evolution tracks. Typical precision is 15% (Brown et al. 2014); the accuracy depends on the choice of stellar evolution tracks (i.e., assumptions about metallicity). Proper motions are equally difficult to measure, because HVSs are distant and they should be on radial trajectories. Expected HVS proper motions are typically $\lesssim$1 mas yr^{-1} and thus cannot be measured with ground based surveys. The only unbound star with a statistically significant proper motion measurement to date is the runaway B star HD 271791, a star that was ejected in the direction of Galactic rotation from the outer disk (Heber et al. 2008). HIP 60350 is another example of a high velocity B star with a significant proper motion measurement, but it is unbound at less than 1σ significance (Irrgang et al. 2010). Here, we present *Hubble Space Telescope (HST)* proper motion measurements for a sample of 16 stars with extreme radial velocities, 12 of which are unbound to the Milky Way in radial velocity alone.

Proper motions are important because they can discriminate between Galactic center and Galactic disk origins. The star US 708 (hereafter HVS 2), for example, is a helium-rich sdO star with a +708 km s^{-1} heliocentric radial velocity (Hirsch et al. 2005). sdO stars are the remnants of low mass stars; helium rich sdO stars are possibly the merger product of two helium white dwarfs (Heber 2009). If HVS 2 were ejected by the central MBH, its velocity vector will point away from the Galactic center. If HVS 2 were ejected by a Type Ia supernova explosion (Justham et al. 2009; Wang & Han 2009), its velocity vector can point from anywhere in the Milky Way.

Generally speaking, lower velocity stars are more likely to be disk runaways. The maximum ejection velocity in the

---

Blaauw (1961) supernova mechanism is the sum of the supernova kick velocity and the orbital velocity of the progenitor binary, or about $250\,\mathrm{km\,s^{-1}}$ for an ejected main-sequence B star (Portegies Zwart 2000). Velocities up to $500\,\mathrm{km\,s^{-1}}$ may be possible for B stars ejected by extremely asymmetric core-collapse supernovae in contact binaries (Tauris 2015). The maximum ejection velocity in the dynamical mechanism depends on the most massive star in the encounter, and can also reach $500\,\mathrm{km\,s^{-1}}$ in extreme scenarios (Leonard 1991; Gvaramadze et al. 2009). Simulations suggest that 99% of dynamical ejections occur at velocities $<200\,\mathrm{km\,s^{-1}}$ (Perets & Subr 2012). We test for the existence of $\sim500\,\mathrm{km\,s^{-1}}$ runaway ejections by including four bound velocity outliers in our sample.

The star HE 0437–5439 (hereafter HVS 3), an unbound 9 $M_\odot$ main-sequence B star located 16 deg from the Large Magellanic Cloud (LMC), presents another puzzle (Edelmann et al. 2005). The lifetime of this star is many times shorter than its flight time from the Milky Way, suggesting an LMC origin. An LMC origin requires a $1000\,\mathrm{km\,s^{-1}}$ ejection, however, and thus an unseen MBH in the LMC (Gualandris & Portegies Zwart 2007). A Milky Way origin, on the other hand, requires that HVS 3 be a blue straggler to account for its lifetime. In other words, the progenitor must have been a binary system ejected at $>800\,\mathrm{km\,s^{-1}}$ that subsequently merged as it traveled away from the Milky Way. A binary MBH could eject stellar binaries as HVSs (Lu et al. 2007), or else a single MBH could eject binaries by triple disruption (Perets 2009). All of these models have very low ejection rates. The LMC and Galactic center origins for HVS 3 differ by $1.5\,\mathrm{mas\,yr^{-1}}$ in proper motion. Using two epochs of *HST* imaging, Brown et al. (2010) found that HVS 3 is moving away from the Milky Way. Irrgang et al. (2013) argue that both Milky Way and LMC origins, given the systematic uncertainties, are consistent with the measurements. A third epoch of imaging is needed.

In principle, *HST* proper-motion measurements have sufficient precision to determine the origin of our unbound stars. Using the best data reduction and measurement techniques, it is possible to achieve 0.01 pixel astrometric precision on well-exposed stars (e.g., Bellini et al. 2014). The Advanced Camera for Surveys (ACS) Wide-Field Channel has 50 mas pixels, and the Wide Field Camera 3 (WFC3) Ultraviolet-visible (UVIS) Channel has 40 mas pixels. For a pair of measurements separated by a 3 yr time baseline, we can thus expect $0.2\,\mathrm{mas\,yr^{-1}}$ precision. We must rely on background galaxies to define our absolute reference frame, however, and both the number and spatial distribution of useful background galaxies introduce a systematic uncertainty to the measurements. In some cases, a sequence of short and long exposures is used to link faint background galaxies to bright HVSs, adding additional uncertainty.

For the sake of clarity, we quote proper motion uncertainties that are the sum in quadrature of the statistical (stellar) and systematic (background galaxy) proper motion uncertainties throughout this paper. Our average total uncertainty is $\pm0.8\,\mathrm{mas\,yr^{-1}}$, a six-fold improvement over existing proper motion measurements.

In Section 2 we define the sample of 12 unbound and four bound stars, and present new spectroscopy and stellar atmosphere fits for the four bound stars. In Section 3 we describe the *HST* imaging, image reduction, and proper motion measurements. Twelve stars have proper motions statistically consistent

with zero, and thus largely radial trajectories. In Section 4 we evaluate the constraints on a Galactic center origin, accounting simultaneously for radial velocity, distance, and proper motion errors. Thirteen stars have trajectories consistent with a Galactic center origin given the measurement errors, while three stars are inconsistent with a Galactic center origin at $>3\sigma$ confidence. In Section 5 we discuss the objects with significant proper motions, the runaway stars HVS 2, B711, and B733. We also update our constraints on HVS 3, consistent with either a LMC or Milky Way origin. We conclude in Section 6.

2. THE SAMPLE

We select our sample of 16 stars for their extreme radial velocities. We targeted all 12 unbound HVSs known prior to 2008 March, plus four bound velocity outliers from the HVS Survey of Brown et al. (2007b). Table 1 lists the coordinates and other observed properties of the stars. We refer to the 12 unbound stars as HVS 1 (Brown et al. 2005), US 708 = HVS 2 (Hirsch et al. 2005), HE 0437–5439 = HVS 3 (Edelmann et al. 2005), HVS 4–HVS 5 (Brown et al. 2006a), HVS 6–HVS 7 (Brown et al. 2006b), HVS 8–HVS 10 (Brown et al. 2007b), and HVS 12–HVS 13 (Brown et al. 2009). We refer to the four bound velocity outliers as B434, B485, B711, and B733, corresponding to their target numbers in the HVS Survey (Brown et al. 2007b).

Detailed analyses of the unbound stars indicate that, except for HVS 2, they are main-sequence B stars at 50–100 kpc distances. This conclusion is based on stellar atmosphere fits to high resolution echelle spectra of HVS 3 (Bonanos et al. 2008; Przybilla et al. 2008a), HVS 5 (Brown et al. 2012a), HVS 7 (Przybilla et al. 2008b), and HVS 8 (López-Morales & Bonanos 2008), and fits to moderate resolution, high signal-to-noise ratio (S/N) spectra of the other HVSs (Brown et al. 2014). Here we describe spectroscopy of the four bound velocity outliers.

2.1. New Spectroscopy

We obtained 6.5 m MMT Blue Channel spectroscopy of the four bound velocity outliers in four different observing runs in 2006 February, 2008 February, 2010 March, and 2014 March. We used the 832 I mm^{-1} grating in 2nd order with a 1 arcsec slit, providing 1.0 Å spectral resolution over the range 3600–4500 Å. In addition, we observed B485 a second time with a 0.75 arcsec slit to test higher 0.75 Å spectral resolution. We paired every observation with a He–Ne–Ar comparison lamp exposure for wavelength calibration. We chose exposure times to achieve S/N = 50–100 per resolution element in the continuum.

We process and extract the 1D spectra using IRAF.[5] We measure radial velocities using the cross-correlation package RVSAO (Kurtz & Mink 1998). We then measure effective temperature T_{eff}, surface gravity $\log g$, and projected rotation $v\sin i$ using stellar atmosphere models as described in Brown et al. (2014). Figure 1 compares the best-fit stellar atmosphere models to the observed spectra. All four bound velocity outliers are late B-type stars, and B733 has significant projected rotational velocity $v\sin i = 240 \pm 30\,\mathrm{km\,s^{-1}}$.

---

[5] IRAF is distributed by the National Optical Astronomy Observatories, which are operated by the Association of Universities for Research in Astronomy, Inc., under cooperative agreement with the National Science Foundation.

3

Table 1
Observed and Derived HVS Properties

ID	R.A., Decl. (J2000)	v_{helio} (km s^{-1})	T_{eff} (K)	log g (cm s^{-2})	$v \sin i$ (km s^{-1})	M_g (mag)	g_0 (mag)	d_{helio} (kpc)	$\mu_{\mathrm{R.A.}}$, $\mu_{\mathrm{Decl.}}$ (mas yr^{-1})	f_{GC}	Ref
HVS 1	9:07:44.99, +02:45:06.9	831.1 ± 5.7	11192 ± 450	3.91 ± 0.20	158 ± 36	−0.36 ± 0.31	19.69 ± 0.023	102 ± 15	+0.08 ± 0.26, −0.12 ± 0.22	0.47	1,13
HVS 2	9:33:20.87, +44:17:05.5	708.0 ± 15.0	44561 ± 675	5.23 ± 0.12	⋯	+2.22 ± 0.30	18.56 ± 0.013	19 ± 2.6	−7.33 ± 0.58, +2.28 ± 0.55	0.00	2
HVS 3	4:38:12.77, −54:33:11.9	723.0 ± 3.0	23000 ± 1000	3.95 ± 0.10	55 ± 2	−2.57 ± 0.30	16.36 ± 0.20	61 ± 10	+0.52 ± 0.58, +1.65 ± 0.57	0.07	3,8,9
HVS 4	9:13:01.00, +30:51:19.9	600.9 ± 6.2	14547 ± 598	4.15 ± 0.21	77 ± 40	−0.71 ± 0.33	18.34 ± 0.023	64 ± 9.8	−0.23 ± 0.36, −0.42 ± 0.36	0.71	4,13
HVS 5	9:17:59.47, +67:22:38.3	545.5 ± 4.3	12000 ± 350	3.89 ± 0.13	133 ± 7	−0.67 ± 0.25	17.58 ± 0.032	45 ± 5.2	+0.55 ± 0.61, −0.44 ± 0.59	0.16	4,12
HVS 6	11:05:57.45, +09:34:39.4	609.4 ± 6.8	12190 ± 537	4.30 ± 0.23	170 ± 55	+0.25 ± 0.27	18.94 ± 0.024	55 ± 6.9	+0.05 ± 0.57, +0.31 ± 0.97	0.33	5,13
HVS 7	11:33:12.13, +01:08:24.8	526.9 ± 3.0	12000 ± 500	3.80 ± 0.10	55 ± 2	−0.95 ± 0.26	17.63 ± 0.015	52 ± 6.4	+1.00 ± 0.82, −0.55 ± 1.04	0.19	5,10
HVS 8	9:42:14.03, +20:03:22.0	499.3 ± 2.9	11000 ± 1000	3.75 ± 0.25	320 ± 60	−0.69 ± 0.40	17.93 ± 0.016	53 ± 9.8	−0.82 ± 1.16, −0.04 ± 0.49	0.39	6,11
HVS 9	10:21:37.08, −00:52:34.7	616.8 ± 5.1	11637 ± 520	3.84 ± 0.21	306 ± 72	−0.71 ± 0.34	18.64 ± 0.023	74 ± 12	−1.26 ± 0.74, −0.25 ± 0.70	0.95	6,13
HVS 10	12:03:37.85, +18:02:50.3	467.9 ± 5.6	11278 ± 524	4.38 ± 0.23	37 ± 60	+0.65 ± 0.24	19.24 ± 0.024	52 ± 5.8	−1.07 ± 0.36, −0.58 ± 0.42	0.86	6,13
HVS 12	10:50:09.60, +03:15:50.6	552.2 ± 6.6	12098 ± 622	4.62 ± 0.28	78 ± 88	+0.55 ± 0.28	19.63 ± 0.024	66 ± 8.5	−0.40 ± 0.36, +0.31 ± 0.34	0.08	7,13
HVS 13	10:52:48.31, −00:01:33.9	569.3 ± 6.1	11054 ± 775	4.00 ± 0.35	238 ± 43	−0.10 ± 0.40	20.01 ± 0.021	105 ± 19	−0.90 ± 0.38, +0.46 ± 0.44	0.03	7,13
B434	11:02:24.37, +02:50:02.8	443.9 ± 2.9	10232 ± 382	3.93 ± 0.20	117 ± 42	+0.06 ± 0.27	18.00 ± 0.016	39 ± 4.8	−1.61 ± 0.28, −0.26 ± 0.42	0.08	6
B485	10:10:18.82, +30:20:28.1	408.1 ± 4.8	16167 ± 542	4.02 ± 0.12	88 ± 69	−1.36 ± 0.30	16.06 ± 0.016	30 ± 4.3	−1.66 ± 0.52, −1.15 ± 0.38	0.50	6
B711	14:20:01.94, +12:44:04.7	273.7 ± 5.4	11004 ± 298	4.27 ± 0.15	60 ± 76	+0.72 ± 0.26	16.92 ± 0.016	17 ± 2.0	−0.96 ± 0.80, +1.55 ± 0.86	0.00	6
B733	14:49:55.58, +31:03:51.3	348.8 ± 2.3	10522 ± 301	4.25 ± 0.14	240 ± 28	+0.87 ± 0.24	15.67 ± 0.020	9 ± 1.0	−1.77 ± 0.79, −3.71 ± 0.89	0.00	6

References. (1) Brown et al. (2005), (2) Hirsch et al. (2005), (3) Edelmann et al. (2005), (4) Brown et al. (2006a), (5) Brown et al. (2006b), (6) Brown et al. (2007b), (7) Brown et al. (2009), (8) Przybilla et al. (2008a), (9) Bonanos et al. (2008), (10) Przybilla et al. (2008b), (11) López-Morales & Bonanos (2008), (12) Brown et al. (2012a), (13) Brown et al. (2014).
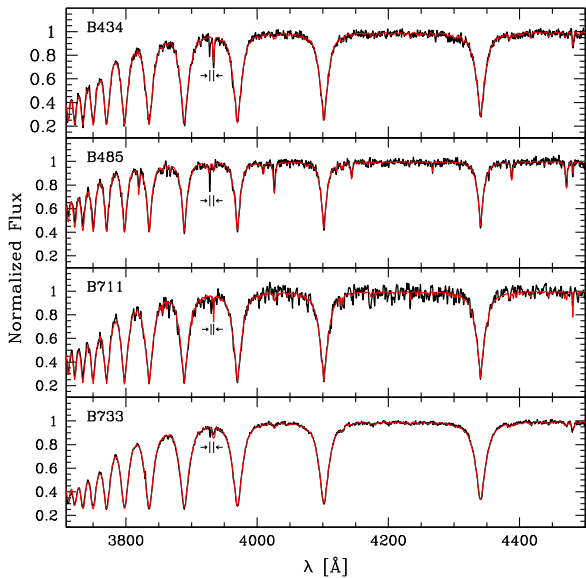
Figure 1. Spectra of the bound velocity outliers, continuum-normalized and shifted to rest-frame (in black), compared to their best-fitting stellar atmosphere model (in red). The wavelength separation between the pair of Ca II $\lambda3933$ lines (marked with arrows), the lefthand one due to local interstellar medium absorption, visibly shows each star's large radial velocity. We use the hydrogen Balmer lines to measure $T_{\rm eff}$, $\log g$, and $v \sin i$.
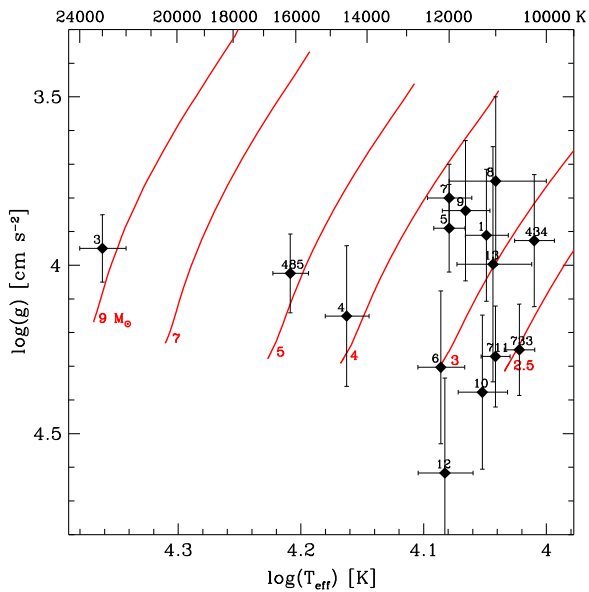

Figure 2. Effective temperature $T_{\rm eff}$ and surface gravity $\log g$ compared with Padova solar metallicity main-sequence tracks (red lines) for our sample of stars. Stars are labeled by their HVS/B identifier number.

2.2. Stellar Parameters

Our sample contains 15 B-type stars plus the sdO star HVS 2. Figure 2 displays the adopted effective temperature $T_{\rm eff}$ and surface gravity $\log g$ for the 15 B-type stars in our sample, plotted in comparison to Padova solar metallicity main-sequence tracks (Girardi et al. 2004; Marigo et al. 2008; Bressan et al. 2012). HVS 2 does not appear because it is a $T_{\rm eff}$ = 45,560 K sdO star. The clumping of stars in Figure 2 reflects the HVS Survey target selection of stars with the colors of 3 $M_\odot$ main-sequence stars.

Notably, all four stars with high resolution echelle spectroscopy are fast rotators. Another five B-type stars have statistically significant $v \sin i \geqslant 150$ km s^{-1} on the basis of our moderate resolution MMT spectroscopy. Fast rotation is the unambiguous signature of a main-sequence B star. For reference, the mean $v \sin i$ of late B-type stars is 150 km s^{-1} (Abt et al. 2002; Huang & Gies 2006). Evolved horizontal branch stars of the same temperature and surface gravity, on the other hand, are slow rotators with $v \sin i < 7$ km s^{-1} (Behr 2003). Thus these B-type stars are main-sequence stars.

We compare the measured stellar atmosphere parameters to Padova main-sequence stellar evolution tracks to estimate luminosities (Girardi et al. 2004; Marigo et al. 2008; Bressan et al. 2012). Propagating the measurement uncertainties through the stellar evolution tracks implies that our luminosity estimates are precise to 30% in luminosity, or 15% in distance. The precision is relatively poor because surface gravity is our primary constraint on evolutionary status, and the luminosities of B stars increase with age.

The choice of stellar evolution tracks is a source of systematic uncertainty. With the exception of HVS 3 and HVS 7, which have solar iron abundance (Przybilla et al. 2008a, 2008b), the metallicity of the HVSs is unconstrained. If the HVSs are systematically metal-rich or metal-poor, our distance estimates could be systematically wrong by ~25% (e.g., Bressan et al. 2012). Given that the HVSs are relatively short-lived main-sequence B stars, however, we consider solar metallicity a reasonable assumption.

We calculate heliocentric distance using the de-reddened g-band point-spread function (PSF) apparent magnitudes from Sloan Digital Sky Survey (SDSS) Data Release 10 (DR10; Ahn et al. 2014), except for HVS 3 which has a V-band measurement (Bonanos et al. 2008). The SDSS magnitudes have a typical precision of 2%; however in some cases the DR10 g-band magnitude differs from previous SDSS data release values by as much as 10%. The SDSS photometry is thus an additional source of uncertainty, but a small fraction of the total error budget.

Table 1 summarizes the measured and derived properties for the 16 stars. We adopt parameters from published echelle spectra when available; otherwise we adopt parameters derived from our MMT spectra. The stellar atmosphere parameters for the four bound velocity outliers are new.

3. PROPER MOTION MEASUREMENTS

3.1. HST Observations

We imaged the 16 stars using the *HST* ACS and WFC3/UVIS instruments starting in 2006 September and ending in 2013 March. We obtained images in a few different ways; Table 2 lists the full set of observations.

We first observed HVS 1–HVS 5 using ACS in 2006 (proposal ID 10824). Each star was allocated one orbit, and was observed with a set of 4–7 dithered exposures. Exposure times were chosen to maximize counts on background galaxies while not saturating the HVSs. We obtained a second epoch of observations with ACS in 2009 (proposal ID 11782). For HVS 1–HVS 4, we then obtained a third epoch of observations using WFC3 (proposal ID 12503). We allocated two orbits of time per star in the third epoch, but dropped HVS 5 because its field

Table 2
List of *HST* Observations

ID	UT Date	Instr	Filter	PA (deg)	Exptime (s)
HVS 1	2006-10-11	ACS	F814W	−80.2	522 × 5
⋯	2009-10-05	ACS	⋯	−82.9	540 × 5
⋯	2013-02-21	WFC3	⋯	−80.2	612 × 8
HVS 2	2006-10-04	ACS	F814W	−56.2	532 × 4
⋯	2009-11-03	ACS	⋯	−56.2	560 × 4
⋯	2012-11-22	WFC3	⋯	142.8	627 × 8
HVS 3	2006-07-08	ACS	F850LP	−145.2	257 × 6
⋯	2009-12-23	ACS	⋯	35.0	300 × 6
⋯	2012-09-01	WFC3	⋯	124.8	388 × 12
HVS 4	2006-11-06	ACS	F814W	−82.0	390 × 5
⋯	2009-11-07	ACS	⋯	−86.0	410 × 5
⋯	2013-02-13	WFC3	⋯	24.8	618 × 8
HVS 5	2006-09-01	ACS	F814W	−26.1	199 × 7
⋯	2009-08-30	ACS	⋯	−25.9	200 × 7
HVS 6	2009-11-07	WFC3	F606W	159.3	290 × 6
⋯	2012-11-19	WFC3	⋯	159.6	466 × 5
HVS 7	2009-12-04	WFC3	F606W	157.5	475 × 3, 90 × 3
⋯	2012-12-05	WFC3	⋯	157.8	531 × 3, 160 × 3
HVS 8	2009-11-17	WFC3	F606W	139.4	460 × 3, 120 × 3
⋯	2012-11-26	WFC3	⋯	138.8	494 × 3, 200 × 3
HVS 9	2009-11-07	WFC3	F606W	151.8	290 × 6
⋯	2012-11-25	WFC3	⋯	152.1	366 × 6
HVS 10	2010-02-23	WFC3	F606W	103.4	379 × 6
⋯	2013-03-06	WFC3	⋯	103.3	609 × 4
HVS 12	2009-11-08	WFC3	F606W	155.2	627 × 4
⋯	2012-11-30	WFC3	⋯	155.2	613 × 4
HVS 13	2009-11-13	WFC3	F606W	154.5	619 × 4
⋯	2012-11-29	WFC3	⋯	154.5	613 × 4
B434	2009-11-06	WFC3	F606W	155.3	580 × 3, 120 × 3
⋯	2012-11-22	WFC3	⋯	155.6	536 × 3, 160 × 3
B485	2009-10-30	WFC3	F606W	161.4	563 × 3, 25 × 3
⋯	2012-11-20	WFC3	⋯	147.8	675 × 3, 35 × 3
B711	2009-12-18	WFC3	F606W	170.5	526 × 3, 50 × 3
⋯	2012-12-16	WFC3	⋯	170.8	608 × 3, 75 × 3
B733	2009-12-12	WFC3	F606W	−173.6	563 × 3, 16 × 3
⋯	2012-12-09	WFC3	⋯	−173.3	653 × 3, 30 × 3

contained few useful background galaxies. The time baseline of observations for HVS 1–HVS 4 is thus about 6.2 yr, and for HVS 5 it is 3.0 yr.

We observed the other 12 stars exclusively with WFC3 beginning in 2009–2010 (proposal ID 11589). Each star was allocated one orbit of time and observed with a set of dithered exposures. For the brightest six stars, however, we divided the exposures into a set of short ≃1 minute and deep ≃10 minute exposures. Our goal was to optimally expose the bright HVSs and faint background galaxies in the short and deep exposures, respectively, and to tie their astrometric frames together using the intermediate brightness stars available in both sets of exposures. In practice, the finite number of intermediate brightness stars limits the accuracy of this approach. We obtained a second epoch of observations with WFC3 in 2012–2013 (proposal ID 12662) in the same way. The time baseline of the observations is 3.0 yr for these 12 stars.

We made an effort to use the same telescope orientation across all epochs of imaging in order to minimize the impact of changes in charge-transfer efficiency (CTE) and errors in the distortion solution. The effects of CTE increase with time as on-orbit radiation damage creates more and more charge traps in the CCD silicon lattice. The result is that star and galaxy

images are trailed along the CCD read-out direction. If we observe in the same orientation in all epochs, the CTE systematic is in the same direction and we minimize its impact on our differential position measurements. Unfortunately, we were unable to use the same guide stars for HVS 2, HVS 3, and HVS 4 in all epochs due to changes in the *HST* guide star catalog. This issue forced a change in orientation, which exacerbates the astrometric effects of CTE. Table 2 lists the position angle (PA), defined as increasing east of due north, for each observation.

3.2. Image Reduction and Analysis

We begin our data reduction procedure by downloading flat-fielded images from the Mikulski Archive for Space Telescopes. Because the CTE correction for WFC3/UVIS images and ACS subarrays is not integrated into the standard pipeline, we run the Anderson & Bedin (2010) pixel-based correction by hand. The CTE correction is calibrated on hot pixels and their charge trails, and is successful at removing the trails behind stars, cosmic rays, and hot pixels, and restoring the flux to the stellar images.

We start our analysis with the first-epoch images. We use empirical models of the ACS and WFC3/UVIS PSFs to measure positions for stars in the CTE-corrected frames of each first epoch exposure. We then correct the positions for geometric distortion using the model in Anderson & King (2006) for ACS and the model in Bellini et al. (2011) for WFC3/UVIS. Finally, we cross identify the stars and define a linear transformation from the distortion-corrected positions of each star in each exposure into the distortion-corrected frame of the first exposure.

Since all of the first-epoch images were taken in a single orbit, we can safely use the stars to define the transformations. This cannot be done for the later epochs, since the stars are all moving, and we need to know the motion of each target star in an inertial frame. Therefore, we use the background galaxies to define the transformation from each exposure into the reference frame. Although all stars can be fit with the same PSF, each galaxy has its own unique distribution of light and must be measured with its own template. An additional complication is that some images were taken at different orientations or with different instruments, such that the PSF for a given object might be different from epoch to epoch, affecting the observed distribution of light. For this reason, we construct templates for each galaxy with a deconvolved model, such that when we fit the template to the pixels in an image, we first convolve it with the PSF appropriate for that location in that detector. This approach ensures that the stars (which are simply delta functions when deconvolved) and galaxies are measured consistently within an exposure.

We construct the star and galaxy templates from the exposures in the first-epoch data set. The transformations (based on the stars) enable us to accurately map the pixels of all exposures into the reference frame. For each source, we collect all the pixels that map to within the 11 × 11 region about each source (galaxies and stars). We then use iterative forward modeling to construct a deconvolved template for each source. The template for the stars is simply a delta function. The template for the galaxies is a smooth empirical image that, when convolved with the PSF, best described the distribution of light in the contributing exposures. We allowed the galaxies

to have an additional point source at their centers, but most did not need one.

We then use these templates, convolved with the appropriate PSF, to measure consistent positions for every source in every exposure in each epoch. We examine the fitting residuals for each source and reject the measurements that were clearly contaminated by cosmic rays or unidentified warm pixels. Measured positions are in the raw frame and must be corrected for geometric distortion, as mentioned above. Next, we use the positions for the galaxies to define the linear transformation from the distortion-corrected frame of each exposure into that of the first exposure of the first epoch. We examine the transformation residuals for each galaxy and reject those galaxies with unreliable and inconsistent positions. This leaves us with 10–15 high quality galaxies for each field. From the residuals, we infer that the transformations are typically good to ±0.93 mas, which corresponds to a 0.31 mas yr^{-1} systematic uncertainty in the reference frame for a 3 yr time baseline. The systematic uncertainty is a noise floor to all of our measurements.

Finally, we use these galaxy-based transformations to map the position for each star in each exposure into the reference frame, and then solve for the proper motions. Mathematically, the proper motion calculation boils down to a linear least squares fit to the x and y positions versus time of observation, which we know exactly. We convert the x and y pixel motions into mas yr^{-1} using the appropriate camera pixel scale, image rotation angle, and time baseline of observations. Proper motion uncertainties are determined from the scatter in x and y positions at each epoch, and added in quadrature to the uncertainty of the galaxy reference frame. Total measurement uncertainties range from ±0.35 mas yr^{-1} for the case of HVS 1, which has a 6.36 yr time baseline of observations, to ±1.33 mas yr^{-1} for the case of HVS 7, which has only 8 useable reference galaxies. Our final proper motion measurements are in Table 1.

3.3. Comparison with Previous Measurements

Our proper motion measurements are a six-fold improvement over previous measurements. One of the most accurate proper motion catalogs available today is the UCAC 4, which covers the entire sky to a depth of $R = 16$ mag (Zacharias et al. 2013). One of our stars, B733, is bright enough to have a UCAC 4 measurement. The UCAC 4 total proper motion for B733, $\mu_{\rm UCAC\,4,B733} = 13.9 \pm 6.6$ mas yr^{-1}, agrees to within 1.5σ of our measurement $\mu_{\rm B733} = 4.1 \pm 1.2$ mas yr^{-1}. Another catalog is PPMXL (Roeser et al. 2010), which combines 2MASS and USNO-B astrometry. Only B733 is bright enough to have a 2MASS measurement, and the PPMXL total proper motion $\mu_{\rm PPMXL,B733} = 6.3 \pm 6.8$ mas yr^{-1} is in perfect agreement with our measurement. The SDSS survey probes much deeper and, when combined with USNO-B astrometry (Monet et al. 2003), provides proper motion measurements for all of our sample except HVS 3. The average SDSS-USNO-B proper motion uncertainty for our stars is ±5.3 mas yr^{-1}, and only one star, HVS 5, has a SDSS proper motion that differs from zero at greater than 1.5σ significance. In contrast, our *HST* measurements have an average proper motion uncertainty of ±0.8 mas yr^{-1}, and thus are 6.6 times more accurate.

3.4. Proper Motions in Context

At first glance, the stars have small proper motions and thus largely radial trajectories. Twelve of the stars have proper motions statistically consistent with zero. Only HVS 2, B434, B485, and B733 have proper motions that differ from zero at better than 3σ significance.

For distant stars, however, the reflex motion caused by the Sun orbiting the Milky Way can dominate the apparent proper motion. The direction and amplitude of solar reflex motion depends on the location and distance of the star. Thus, a correct interpretation of the proper motion measurements requires that we calculate trajectories.

As a first step, we adopt a fixed distance, radial velocity, right ascension, and declination (those listed in Table 1) for each star, and then calculate each trajectory backward in time for all possible proper motions that cross the Galactic plane. We use the Kenyon et al. (2014) three component bulge-disk-halo potential model for the trajectory calculations. This potential model uniquely fits observed mass measurements from the Galactic center to the outer halo, but was originally constructed for a 220 km s^{-1} circular velocity (Kenyon et al. 2008). Updating the disk mass $M_d = 6 \times 10^{10}$ $M_\odot$ and disk radial scale length $a_d = 2.75$ kpc yields a flat rotation curve of 235 km s^{-1} consistent with the most recent circular velocity measurements (Reid et al. 2014). We refer to this potential model as the Kenyon et al. (2014) model, and use it in all of our trajectory calculations.

Assuming a fixed distance, radial velocity, right ascension, and declination (those listed in Table 1), Figure 3 compares our measured proper motions to the results of our trajectory calculations. The green and blue ellipses show the locus of proper motions with trajectories that pass within 8 and 20 kpc, respectively, of the Galactic center. Statistically, all of our stars have proper motions consistent with a Milky Way origin. Our strongest constraints are for the three closest stars that have significantly non-zero proper motions: HVS 2, B711, and B733. To evaluate the likelihood of a more exact origin requires that we account for all of the measurement errors, in proper motion, radial velocity, and distance.

4. ORIGIN OF HYPERVELOCITY STARS

With proper motions in hand, we can now address the question of origin. We expect that the fastest unbound stars, as discussed above, are most likely HVSs ejected by the MBH in the Galactic center. Lower velocity stars can be explained by alternative scenarios, such as runaway ejections from the disk. Importantly, runaways with unbound speeds are most likely to be those stars ejected in the direction of Galactic rotation from the outer disk (Heber et al. 2008; Bromley et al. 2009; Kenyon et al. 2014) Thus we can distinguish between the runaway and MBH ejection scenarios if we know where the trajectories of our stars cross the Galactic plane.

The stars in our sample were selected on the basis of their extreme radial velocities. Their trajectories in the Galactic frame will therefore point away from the Sun unless they have proper motions that significantly deviate from the Solar reflex motion.

In reality, the errors in proper motion are too large to pinpoint the location of ejection with the desired accuracy. To put the measurement uncertainties in context, consider a star's tangential velocity $v_{\rm tan} = 4.74\,d\mu$, where d is the heliocentric
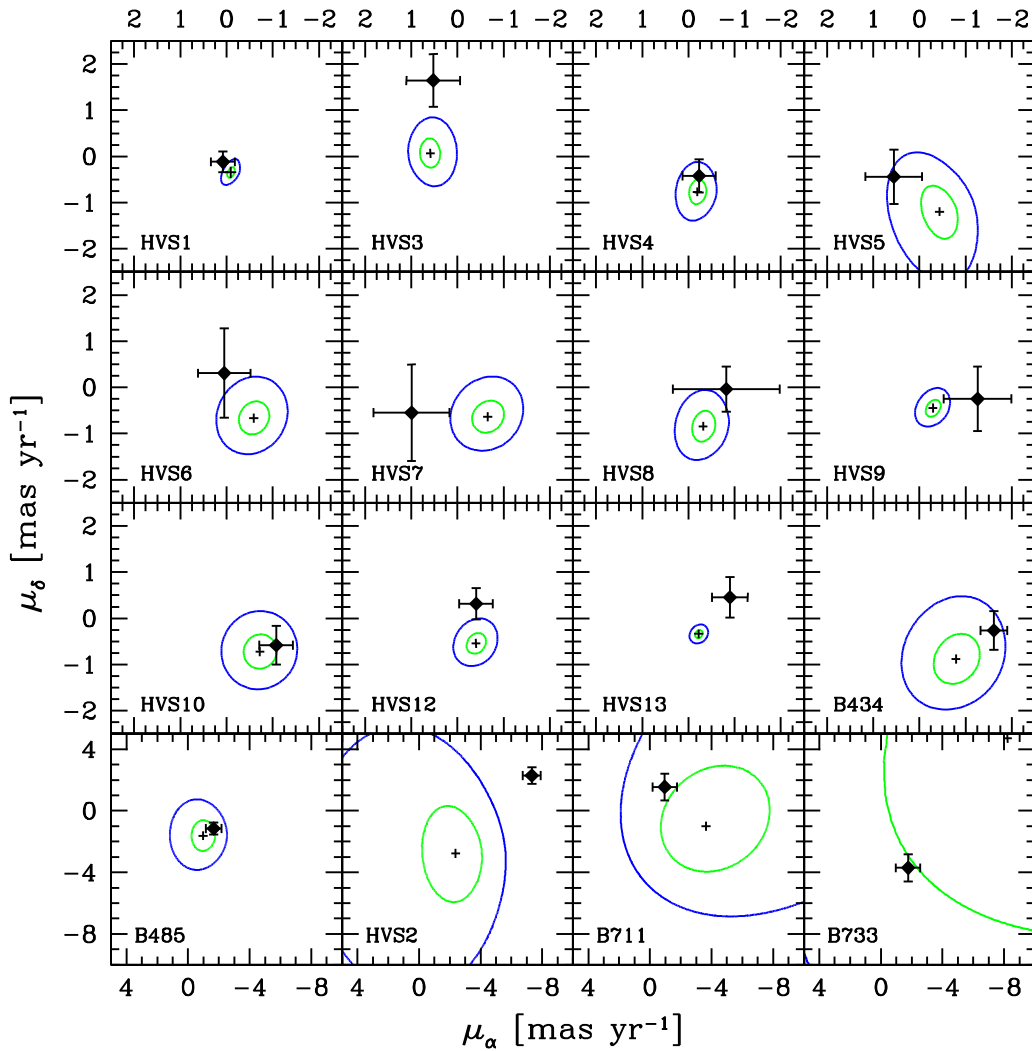
Figure 3. Proper motions in context: assuming a fixed distance, radial velocity, right ascension, and declination for each star (those listed in Table 1), we compare the measured proper motions (points with errorbars) to the locus of trajectories that pass within 8 kpc (green ellipse) and 20 kpc (blue ellipse) of the Galactic center. Trajectories that pass through the Galactic center are marked by a +. All calculations use the Kenyon et al. (2014) potential model. To evaluate the likelihood of origin requires that we account for all of the measurement errors, as seen in Figure 4.

distance in Kiloparsecs and μ is the proper motion in mas yr^{-1}. The typical star in our sample has a median distance of 50 kpc and a proper motion error of ± 0.8 mas yr^{-1}, thus an error in tangential velocity of ± 190 km s^{-1}. For the median total space velocity of 650 km s^{-1}, the uncertainty in the angle of trajectory is $\pm 16°$. Over a distance of 50 kpc, the uncertainty in position is thus ± 15 kpc.

While we would like to test whether an observed trajectory goes exactly through the Galactic center, the errors preclude locating a trajectory to any one point. Instead, we use the measurements to try to disprove a Galactic center origin. Our approach is to calculate the statistical consistency of the measurements with a Galactic center trajectory. We obtain the same answer to this question whether we calculate trajectories from the star backward in time or from the Galactic center forward in time, because the proper motion and distance errors are the same either way. Measurement errors make either the Galactic center or the star look very blurry.

We use a Monte Carlo calculation to account for all of the measurement uncertainties, and visualize the results in a distribution of Galactic plane-crossing locations. For each star,

we draw 1,000,000 current velocities and distances assuming that the measured proper motion, radial velocity, and distance have Gaussian random uncertainties. We then calculate each trajectory backward in time and record where it crosses the Galactic plane.

Figure 4 presents the resulting distribution of Galactic plane-crossing locations for our sample. A black star shows the present location of each star, and a solid black line shows its trajectory. Magenta and cyan ellipses show the 1σ and 2σ likelihood plane-crossing regions, respectively. We determine these regions by calculating the density of plane-crossing locations in bins of X and Y, and solving for the density level thresholds that contain 68.26 and 95.44% of all the crossings within them. The contours are centered on the mode of the plane-crossing distributions, which can differ from the mean trajectory (black line). Drawing both a large distance and a large proper motion can result in a very large tangential motion and thus an extreme plane-crossing location. We discard those trajectories that fail to cross the Galactic plane within the main sequence lifetime of each star. For reference, a 3 $M_\odot$ star has a 365 Myr main sequence lifetime in the Padova tracks;
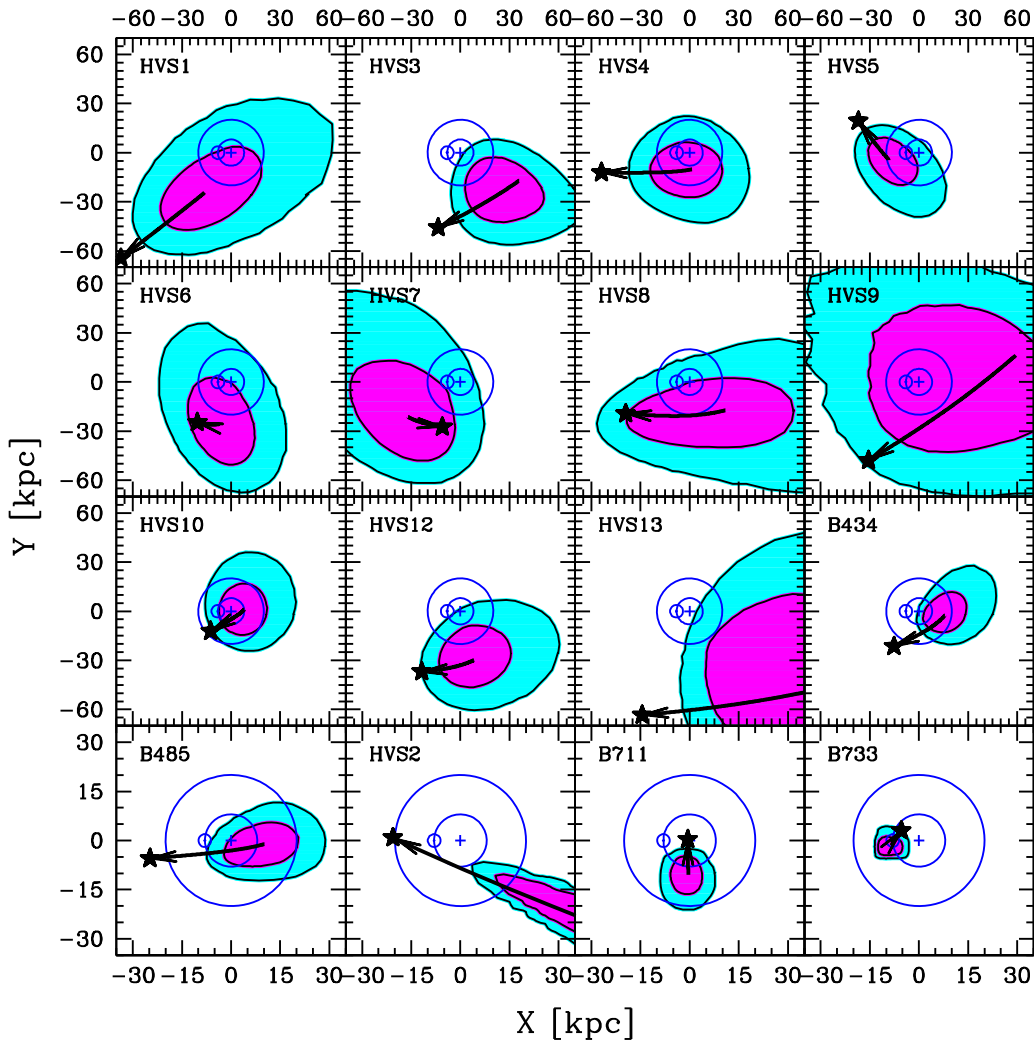
Figure 4. Distribution of Galactic plane-crossing locations for each star, calculated assuming Gaussian random uncertainties in the measured proper motions, radial velocities, and distances. For context, the large blue circles show the $R = 8$ solar circle and $R = 20$ kpc outer edge of the disk. The Sun is at $X = -8$ kpc (small blue circle), the Galactic center is marked with +, and the disk rotates clockwise in this plot. Black stars show the present location of each star, and the solid black lines with arrows show their trajectories. Magenta and cyan ellipses are the 1 and 2σ likelihood regions where the stars cross the Galactic plane.

for the special cases HVS 2 and HVS 3, we allow flight times of 1 Gyr and 100 Myr, respectively. These flight time constraints exclude fewer than 1% of trajectories for most of the sample.

Because distance and proper motion are the most uncertain parameters, the size and shape of the Galactic plane-crossing likelihood regions are driven by the distance and proper motion uncertainties. There is no visible change in the Galactic plane-crossing likelihood regions if we use a different potential model, specifically the one based on Gnedin et al. (2005) and updated in Gnedin et al. (2014). Similarly, a triaxial halo potential model, like that expected from cosmological simulations, changes the trajectories very little.

Half of our stars have trajectories that formally cross the Galactic plane at $R > 20$ kpc, outside of the Milky Way disk, but all of our stars include a part of the Milky Way within their 1σ plane-crossing likelihood regions. Only one star, HVS 7, has a trajectory moving opposite to the direction of Galactic rotation. HVS 7 is also our most uncertain proper motion measurement. Because a counter-rotation trajectory requires an unphysically large Galactic plane ejection velocity, we consider

the astrometric link between the short- and long-exposures of HVS 7 suspect. Many more stars, including HVS 1, HVS 4, HVS 10, and B485, have very radial trajectories.

We reject the Galactic center origin hypothesis if the Galactic center trajectory falls outside the 3σ ($f_{GC} < 0.0026$) threshold of the distribution (Figure 4). The value of f_{GC} is determined as the fraction of all possible orbits with the density of plane-crossings below the value at the GC bin ($X = 0$, $Y = 0$). This respresents the consistency of the Galactic center trajectory with the measurement uncertainties. By this estimate, 13 of our stars are consistent with a Galactic center origin within about the 2σ ($f_{GC} \geqslant 0.046$) confidence level. As a sanity check, we obtain essentially the same result if we ignore the potential model and simply compare a perfectly radial trajectory against the observed tangential velocities. Tangential velocity error drives the uncertainty. Only the stars HVS 2, B711, and B733 have measurements inconsistent with a Galactic center origin at $>3\sigma$ ($f_{GC} < 0.0026$) confidence: they are runaways. We discuss these objects in more detail below.

5. INDIVIDUAL OBJECTS

5.1. HVS 2

HVS 2 is a helium rich sdO star with a $708 \pm 15 \ \mathrm{km \ s^{-1}}$ heliocentric radial velocity (Hirsch et al. 2005). The two proposed explanations for its extreme motion are an ejection by the central MBH (Hirsch et al. 2005; Perets 2009) or a Type Ia supernova explosion (Justham et al. 2009; Wang & Han 2009).

HVS 2 has a significant proper motion of $(\mu_{\mathrm{R.A.}}, \mu_{\mathrm{Decl.}})$ $= (-7.33 \pm 0.58, 2.28 \pm 0.55) \ \mathrm{mas \ yr^{-1}}$. Our measurement is based on three epochs of imaging and therefore has a very well understood error distribution. Given HVS 2's $18.5 \pm 2.6 \ \mathrm{kpc}$ heliocentric distance (Hirsch et al. 2005), the observed proper motion corresponds to a $673 \pm 118 \ \mathrm{km \ s^{-1}}$ tangential motion. HVS 2's tangential motion is quite similar to its radial velocity. Thus its space motion in the rest frame of the Milky Way is almost exactly $1000 \ \mathrm{km \ s^{-1}}$ (!).

The direction of HVS 2's proper motion takes its trajectory across the Galactic plane at $R = 76.5 \ \mathrm{kpc}$. This result implies that HVS 2 originates from the stellar halo, possibly launched by a Type Ia supernova explosion as proposed by Justham et al. (2009) and Wang & Han (2009). If HVS 2's distance and proper motion are 1σ smaller, however, its tangential motion is less extreme and it crosses the Galactic plane around $R = 20 \ \mathrm{kpc}$ (see Figure 4). Thus an ejection from the disk is a viable possibility.

A Galactic center origin for HVS 2, on the other hand, is ruled out at greater than 3σ confidence. HVS 2's closest approach to the Galactic center, given the measurement errors, is $R = 4.5 \ \mathrm{kpc}$ among our 1,000,000 Monte Carlo trajectory calculations. In other words, the extreme velocity of HVS 2 cannot be explained by a dynamical interaction via gravitational interaction with the central MBH. Instead, it is an example of a hyper-runaway star.

Wang & Han (2009) perform ejection calculations for helium star companions to white dwarfs that explode in Type Ia supernovae. In this model, the helium stars receive a kick perpendicular to their orbital velocity for total ejection velocities of 500–$650 \ \mathrm{km \ s^{-1}}$. Similarly, Geier et al. (2013) calculate a $600 \ \mathrm{km \ s^{-1}}$ velocity from their Type Ia supernova ejection model. Given these ejection velocities, the Type Ia supernova model cannot explain HVS 2's $1000 \ \mathrm{km \ s^{-1}}$ motion with a disk ejection; HVS 2's trajectory is not even in the direction of Galactic rotation (Figure 4). Tauris (2015)'s aysmmetric core-collapse supernova model can produce $1000 \ \mathrm{km \ s^{-1}}$ velocities for low mass stars. However, there would not be enough time for a low mass star to evolve into an sdO star before its core-collapse companion launches it out of the Galaxy. The remaining possibility is that HVS 2 was launched by a Type Ia supernova from a halo binary traveling at $\sim 400 \ \mathrm{km \ s^{-1}}$ in its current direction of motion.

Alternative origins seem less likely. For example, Abadi et al. (2009) propose that the tidal disruption of a dwarf galaxy can explain unbound stars. This mechanism requires the close peri-center passage of a fairly massive $> 10^{10} \ M_{\odot}$ dwarf to produce unbound stars (Piffl et al. 2011). The non-Galactic-center trajectory of HVS 2, plus the absence of other unbound stars around it, would appear to rule out the dwarf galaxy tidal debris origin. Additional evidence for a Type Ia supernova explosion, perhaps found in the abundance pattern of HVS 2's stellar atmosphere, would better support the supernova origin picture.

5.2. B711 and B733

B711 and B733 are both bound B-type stars at modest 9–17 kpc distances, and thus plausible candidates for being runaway B stars ejected from the disk. Alternatively, they could be failed HVSs on bound trajectories from the Galactic center. Their radial velocities in the Galactic frame are 290 and $440 \ \mathrm{km \ s^{-1}}$, respectively. In the absence of a positive $v \sin i$ measurement for B711, it is also possible that B711 could be an evolved low mass star (i.e., a hot horizontal branch star) orbiting in the stellar halo. The fact that B733 is a rapidly rotating $2.5 \ M_{\odot}$ main-sequence star with a $349 \ \mathrm{km \ s^{-1}}$ heliocentric radial velocity, however, requires that it was ejected from a location in the Galaxy with recent star formation.

We measure proper motions that point to a disk runaway origin for both stars. The stars formally cross the Galactic plane at $R = 10 \ \mathrm{kpc}$ (Figure 4). A Galactic center origin is ruled out at greater than 3σ confidence for both stars.

The trajectories of B711 and B733 cross the Galactic plane at angles nearly perpendicular to Galactic rotation, however, implying disk ejection velocities of 533 and $441 \ \mathrm{km \ s^{-1}}$. The supernova ejection mechanism is able to achieve $500 \ \mathrm{km \ s^{-1}}$ velocities for main-sequence stars only in extreme scenarios (Tauris 2015). The dynamical ejection mechanism can achieve $500 \ \mathrm{km \ s^{-1}}$ velocities for main-sequence stars but requires 3-body interactions with contact binaries containing $100 \ M_{\odot}$ stars (Gvaramadze et al. 2009; Gvaramadze & Gualandris 2011). Stars with $100 \ M_{\odot}$ are rare and short-lived. Simulations suggest that perhaps 0.1% of dynamical ejections reach $500 \ \mathrm{km \ s^{-1}}$ velocities (Perets & Subr 2012). The upshot is that we expect to find more Galactic center ejections than disk runaway ejections at these speeds (Bromley et al. 2009; Perets & Subr 2012; Kenyon et al. 2014). The fact that B711 and B733 are $\simeq 500 \ \mathrm{km \ s^{-1}}$ disk runaway ejections is thus quite intriguing.

Because extreme runaway ejections require massive stars with relatively short lifetimes, we expect B711 and B733 to have flight times similar to their stellar ages. Our proper motions correspond to trajectories with 20–40 Myr flight times from the disk. Our spectroscopic $\log g$ measurements favor young ages for both B711 and B733 (see Figure 2), however the uncertainties are large and no statistically meaningful constraint is currently possible. High resolution echelle spectroscopy of B711 and B733 would thus be very interesting. B733 is clearly a main-sequence star on the basis of its rapid rotation, and its trajectory is thus evidence for an extreme stellar dynamical ejection from the disk like that seen for HD 271791 (Heber et al. 2008) and HIP 60350 (Irrgang et al. 2010).

5.3. HVS 3

HVS 3 is the unbound $9 \ M_{\odot}$ main-sequence B star near the LMC on the sky (Edelmann et al. 2005). If HVS 3 comes from the LMC, then its speed is evidence for a MBH hidden somewhere in the LMC (Gualandris & Portegies Zwart 2007). If HVS 3 comes from the Milky Way, then its speed and stellar nature are evidence of a former binary HVS ejection (Lu et al. 2007; Perets 2009). Both origins are unlikely in terms of ejection rates.

In 2010, we published a proper motion for HVS 3 that pointed to a Milky Way origin (Brown et al. 2010). This measurement was based on two epochs of ACS imaging with a
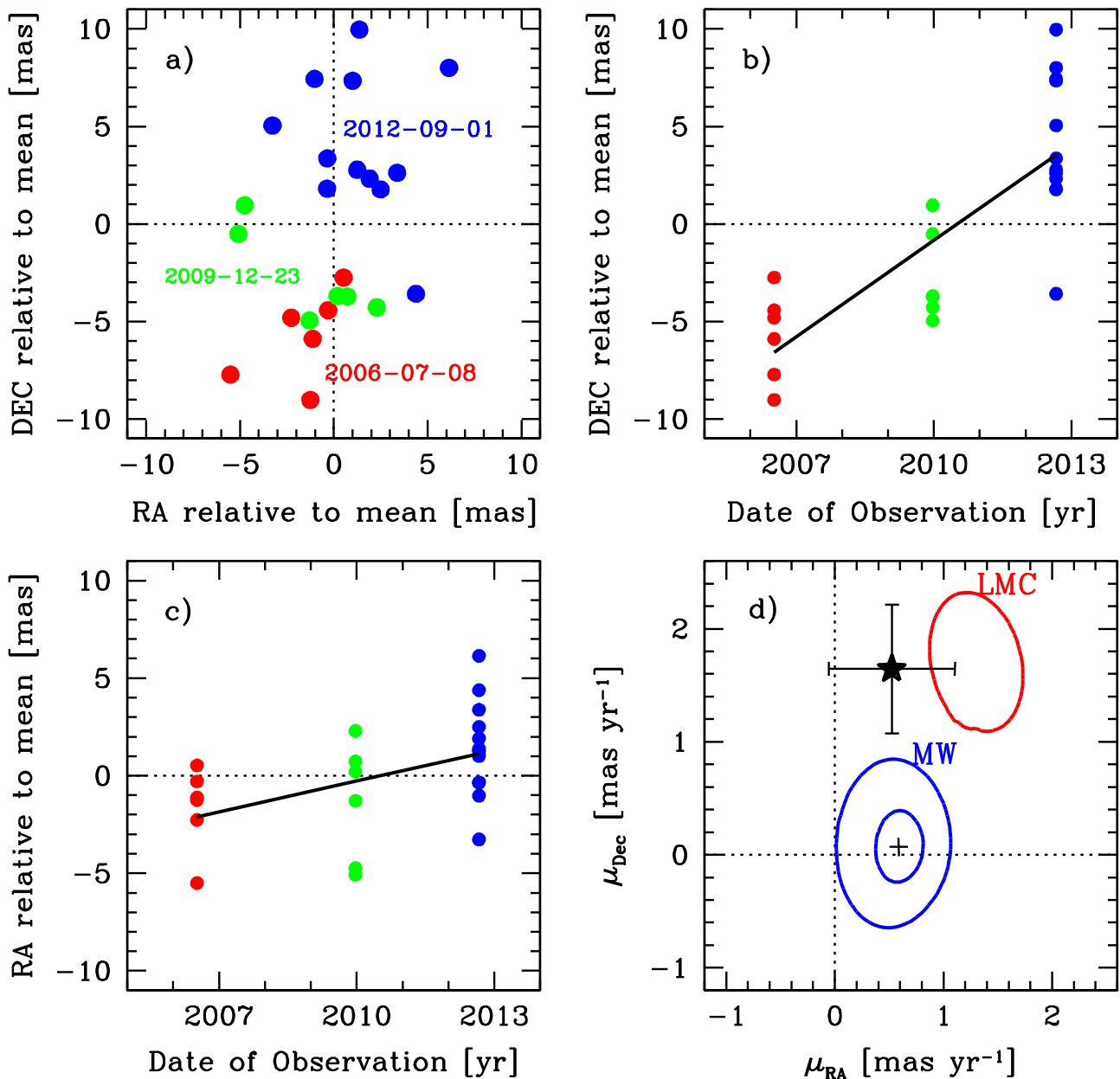
Figure 5. (a) HVS 3 position measurements plotted relative to the mean; we label epoch 1 red, epoch 2 green, and epoch 3 blue. (b) Decl. positions vs. date of observation; solid line is the linear least squares fit to the data. (c) Same as (b) but for R.A. (d) Proper motion (star with errorbars) compared to the locus of HVS 3 proper motions with trajectories that pass with 3 kpc of the LMC (red ellipse) and within 8 and 20 kpc of the Milky Way (blue ellipses). The ellipses are calculated for a fixed HVS 3 distance; accounting for the distance error, HVS 3 is consistent with both LMC and Milky Way origins at the 1σ level.

3.46 yr time baseline. The readout direction of the ACS CCD was unfortunately aligned with the Milky Way-LMC direction, however, and added an additional systematic uncertainty. We now have a third epoch of WFC3 imaging, obtained at an orientation angle 90 deg from the previous data sets, that doubles our time baseline. Our expectation is that HVS 3's intrinsic motion now dominates the errors. We re-process and re-analyze the epoch 1 and 2 data in the same way as the epoch 3 data, so that everything is in a common reference frame.

Figure 5 presents the results. We plot in panel (a) the position of HVS 3, relative to its mean position, as measured in each individual image. Different epochs are identified by color, and the scatter in positions reflects the underlying precision of our measurements. We observe that HVS 3 moves 10.6 ± 5.0 mas, or 0.27 WFC3 pixels, in 6.15 yr. This motion is quantified

in figure panels (b) and (c), which plot the R.A. and decl. positions of HVS 3 versus time. The solid lines in each panel show the linear least squares fit to the measurements. The proper motion of HVS 3 is $(\mu_{R.A.}, \mu_{Decl.}) = (0.52 \pm 0.58, 1.65 \pm 0.57)$ mas yr^{-1}.

As fate would have it, our HVS 3 proper motion corresponds to a physical trajectory that passes in-between the Milky Way and LMC. Figure 5 panel (d) is identical to Figure 3 except that we now draw the locus of HVS 3 proper motions with trajectories that pass within 3 kpc of the LMC (red ellipse). A 3 kpc radius encompasses the full extent of the LMC bar and all of the young clusters proposed by Gualandris & Portegies Zwart (2007) for the origin of HVS 3. We determine HVS 3's distance to the LMC in Figure 5 assuming that the LMC has a mass of $2 \times 10^{10} M_\odot$ moving on an orbit that reproduces the

line-of-sight velocity from van der Marel (2001) and the proper motion from Kallivayalil et al. (2006, 2013) in our Milky Way potential model. If we account for the uncertainties in HVS 3 and LMC distances, then both LMC and Milky Way origins are consistent with the measurements at the 1σ level.

The ambiguity on origin is driven by our epoch 3 measurements, which exhibit a larger shift, and scatter, in position than seen in epochs 1 and 2. This result is visually apparent in Figure 5. Fitting only the epoch 1 and 2 measurements yields $(\mu_{R.A.}, \mu_{Decl.}) = (0.10, 0.89)$ mas yr^{-1}, in 1σ agreement with our previously published value (Brown et al. 2010). Fitting only epoch 2 and 3 measurements, on the other hand, yields $(\mu_{R.A.}, \mu_{Decl.}) = (1.01, 2.52)$ mas yr^{-1}. Clearly, the third epoch drives the proper motion to larger values, and thus causes HVS 3's trajectory to move away from the Milky Way in physical space.

We repeat our measurement and analysis for HVS 3 using only the five best galaxies and obtain essentially the same result. Our reference frame thus appears robust. We speculate that the F850LP filter, chosen to maximize S/N on the background galaxies while not saturating the bright blue star, may be partly to blame. The F850LP filter has a less well-calibrated distortion solution than the F814W and F606W filters, which were used for all of our other observations. The other HVSs with three epochs of data all have less scatter between epochs: the proper motions derived from epochs 1 and 2 and derived from epochs 2 and 3 agree at the 1σ level, except for the decl. motion of HVS 2 that differs by 2σ. Residual CTE systematic error is also a possible problem for the HVS 3 observations. Answering the question of HVS 3's origin will ultimately require a proper motion measurement with a longer time baseline of observations, or else a better instrument like *Gaia*.

6. CONCLUSION

We present *HST* proper motion measurements for 16 stars with extreme radial velocities, 12 of which are unbound to the Milky Way. On the basis of spectroscopic stellar atmosphere fits, our sample consists of 15 main-sequence B stars and one helium-rich sdO star located at 10–100 kpc distances in the stellar halo. We expect that the fastest stars are likely HVSs ejected by the central MBH, and that the lower velocity stars may be runaways ejected from the Milky Way disk.

We process our images using the best geometric distortion solutions, CTE corrections, and empirical PSF fits. Our final proper motions have an average uncertainty of ±0.8 mas yr^{-1}, a six-fold improvement over previous measurements. Twelve of our stars have proper motions consistent with zero, and thus largely radial trajectories.

Given the uncertainties in proper motion and distance, the data allow for a wide range of origin locations. We calculate the statistical consistency of the data with a Galactic center trajectory in an attempt to disprove the Galactic center origin hypothesis. We find that a Galactic center trajectory remains consistent with the measurements for 13 of our stars within the 2σ confidence level. Only the stars HVS 2, B711, and B733 are inconsistent with a Galactic center origin at $>3\sigma$ confidence, and thus runaways.

HVS 2 is an unbound sdO star whose trajectory points from the stellar halo, possibly explained by a Type Ia supernova explosion as proposed by Justham et al. (2009) and Wang & Han (2009). Its 1000 km s^{-1} motion is in some tension with the supernova ejection model, but can be explained if HVS 2 was ejected from a halo orbit. B711 and B733, on the other hand, are B stars with trajectories that clearly point from the stellar disk. These two stars are thus runaway stars, and their trajectories provide strong evidence for $\sim$500 km s^{-1} ejections from the disk.

Our third epoch of imaging for HVS 3, the unbound 9 $M_\odot$ B star near the LMC, yields a larger proper motion than previously measured (Brown et al. 2010) and thus a trajectory further from the Milky Way. Accounting for the uncertainty in HVS 3's distance, its trajectory is now equally consistent with a Milky Way and LMC origin.

In the future, better constraints on HVS trajectories and origin will come from improved proper motion measurements. Doubling the amount of spectra will not significantly improve distance estimates, for example, but doubling the time baseline of imaging will in principle double the precision of the proper motions. Even better, in 2017 *Gaia* will begin releasing proper motions for all of the HVSs. *Gaia*'s predicted precision ranges from ±0.03 mas yr^{-1} for 16th mag stars like HVS 3 and B733, to ±0.3 mas yr^{-1} for a 20th mag star like HVS 1, and with improved accuracy compared to our measurements. *Gaia* will thus provide interesting constraints for all of the known HVSs.

If the unbound HVSs are indeed ejected from the Galactic center, we can use their trajectories to probe the shape and orientation of the Milky Way's dark matter halo (Gnedin et al. 2005). HVSs are effective test particles that traverse the Galaxy to $\sim$100 kpc distances. If the Galactic potential is triaxial, as predicted by cold dark matter simulations, the present motion of HVSs must deviate from being precisely radial. With a sufficient number of HVSs in different directions on the sky, and proper motions accurate to better than 0.1 mas yr^{-1}, it may be possible to measure the two axis ratios and three direction angles of the triaxial halo.

REFERENCES

Abadi, M. G., Navarro, J. F., & Steinmetz, M. 2009, ApJL, 691, L63
Abt, H. A., Levato, H., & Grosso, M. 2002, ApJ, 573, 359
Ahn, C. P., Alexandroff, R., Allende Prieto, C., et al. 2014, ApJS, 211, 17
Anderson, J., & Bedin, L. R. 2010, PASP, 122, 1035
Anderson, J., & King, I. R. 2006, PSFs, Photometry, and Astronomy for the ACS/WFC, Tech. rep., STScI
Behr, B. B. 2003, ApJS, 149, 101
Bellini, A., Anderson, J., & Bedin, L. R. 2011, PASP, 123, 622
Bellini, A., Anderson, J., van der Marel, R. P., et al. 2014, ApJ, 797, 115
Blaauw, A. 1961, BAN, 15, 265
Bonanos, A. Z., López-Morales, M., Hunter, I., & Ryans, R. S. I. 2008, ApJL, 675, L77
Bressan, A., Marigo, P., Girardi, L., et al. 2012, MNRAS, 427, 127
Bromley, B. C., Brown, W. R., Geller, M. J., & Kenyon, S. J. 2009, ApJ, 706, 925
Brown, W. R., Anderson, J., Gnedin, O. Y., et al. 2010, ApJL, 719, L23

Brown, W. R., Cohen, J. G., Geller, M. J., & Kenyon, S. J. 2012, ApJL, 754, L2
Brown, W. R., Cohen, J. G., Geller, M. J., & Kenyon, S. J. 2013, ApJ, 775, 32
Brown, W. R., Geller, M. J., & Kenyon, S. J. 2009, ApJ, 690, 1639
Brown, W. R., Geller, M. J., & Kenyon, S. J. 2012, ApJ, 751, 55
Brown, W. R., Geller, M. J., & Kenyon, S. J. 2014, ApJ, 787, 89
Brown, W. R., Geller, M. J., Kenyon, S. J., & Kurtz, M. J. 2005, ApJL, 622, L33
Brown, W. R., Geller, M. J., Kenyon, S. J., & Kurtz, M. J. 2006, ApJL, 640, L35
Brown, W. R., Geller, M. J., Kenyon, S. J., & Kurtz, M. J. 2006, ApJ, 647, 303
Brown, W. R., Geller, M. J., Kenyon, S. J., Kurtz, M. J., & Bromley, B. C. 2007, ApJ, 660, 311
Brown, W. R., Geller, M. J., Kenyon, S. J., Kurtz, M. J., & Bromley, B. C. 2007, ApJ, 671, 1708
Edelmann, H., Napiwotzki, R., Heber, U., Christlieb, N., & Reimers, D. 2005, ApJL, 634, L181
Geier, S., Marsh, T. R., Wang, B., et al. 2013, A&A, 554, A54
Girardi, L., Grebel, E. K., Odenkirchen, M., & Chiosi, C. 2004, A&A, 422, 205
Gnedin, O. Y., Gould, A., Miralda-Escudé, J., & Zentner, A. R. 2005, ApJ, 634, 344
Gnedin, O. Y., Ostriker, J. P., & Tremaine, S. 2014, ApJ, 785, 71
Gualandris, A., & Portegies Zwart, S. 2007, MNRAS, 376, L29
Gvaramadze, V. V., & Gualandris, A. 2011, MNRAS, 410, 304
Gvaramadze, V. V., Gualandris, A., & Portegies Zwart, S. 2009, MNRAS, 396, 570
Heber, U. 2009, ARA&A, 47, 211
Heber, U., Edelmann, H., Napiwotzki, R., Altmann, M., & Scholz, R.-D. 2008, A&A, 483, L21
Hills, J. G. 1988, Natur, 331, 687
Hirsch, H. A., Heber, U., O'Toole, S. J., & Bresolin, F. 2005, A&A, 444, L61
Huang, W., & Gies, D. R. 2006, ApJ, 648, 580

Irrgang, A., Przybilla, N., Heber, U., Nieva, M. F., & Schuh, S. 2010, ApJ, 711, 138
Irrgang, A., Wilcox, B., Tucker, E., & Schiefelbein, L. 2013, A&A, 549, A137
Justham, S., Wolf, C., Podsiadlowski, P., & Han, Z. 2009, A&A, 493, 1081
Kallivayalil, N., van der Marel, R. P., Alcock, C., et al. 2006, ApJ, 638, 772
Kallivayalil, N., van der Marel, R. P., Besla, G., Anderson, J., & Alcock, C. 2013, ApJ, 764, 161
Kenyon, S. J., Bromley, B. C., Brown, W. R., & Geller, M. J. 2014, ApJ, 793, 122
Kenyon, S. J., Bromley, B. C., Geller, M. J., & Brown, W. R. 2008, ApJ, 680, 312
Kurtz, M. J., & Mink, D. J. 1998, PASP, 110, 934
Leonard, P. J. T. 1991, AJ, 101, 562
López-Morales, M., & Bonanos, A. Z. 2008, ApJL, 685, L47
Lu, Y., Yu, Q., & Lin, D. N. C. 2007, ApJL, 666, L89
Marigo, P., Girardi, L., Bressan, A., et al. 2008, A&A, 482, 883
Monet, D. G., Levine, S. E., Canzian, B., et al. 2003, AJ, 125, 984
Perets, H. B. 2009, ApJ, 698, 1330
Perets, H. B., & Subr, L. 2012, ApJ, 751, 133
Piffl, T., Scannapieco, C., Binney, J., et al. 2014, A&A, 562, A91
Piffl, T., Williams, M., & Steinmetz, M. 2011, A&A, 535, A70
Portegies Zwart, S. F. 2000, ApJ, 544, 437
Poveda, A., Ruiz, J., & Allen, C. 1967, BOTT, 4, 860
Przybilla, N., Nieva, M. F., Heber, U., et al. 2008, A&A, 480, L37
Przybilla, N., Nieva, M. F., Tillich, A., et al. 2008, A&A, 488, L51
Reid, M. J., Menten, K. M., Brunthaler, A., et al. 2014, ApJ, 783, 130
Roeser, S., Demleitner, M., & Schilbach, E. 2010, AJ, 139, 2440
Tauris, T. M. 2015, MNRAS, 448, L6
van der Marel, R. P. 2001, AJ, 122, 1827
Wang, B., & Han, Z. 2009, A&A, 508, L27
Zacharias, N., Finch, C. T., Girard, T. M., et al. 2013, AJ, 145, 44
Zheng, Z., Carlin, J. L., Beers, T. C., et al. 2014, ApJL, 785, L23